An Inductive Power Transfer Charging System With a Multiband Frequency Tracking Control for Misalignment Tolerance

Zhuhaobo Zhang, *Student Member, IEEE*, Shaoting Zheng, *Student Member, IEEE*, Shiying Luo, *Student Member, IEEE*, Dehong Xu, *Fellow, IEEE*, Philip T. Krein, *Life Fellow, IEEE*, and Hao Ma, *Senior Member, IEEE*

***Abstract*—A charging strategy that transitions from constant current (CC) mode to constant voltage (CV) mode is typical for lithium batteries. This presents design challenges for inductive power transfer (IPT) chargers to achieve high efficiency. In this article, a multiband frequency tracking control is proposed to match CC and CV modes and to mitigate misalignment. As in prior work, two load-independent frequencies f_{CC} and f_{CV} are used for respective CC and CV outputs. Unity power factor can be achieved when fully aligned. For misalignment cases, two narrow frequency bands around f_{CC} are selected for control to deliver target output currents and limit reactive power. The duty ratio of the inverter is controlled to set target output voltages. A single-stage IPT system with a series *LCC* topology is analyzed. The proposed control has advantages of narrow operating frequency ranges, high misalignment tolerance, direct design procedures, and high efficiency in both CC and CV modes. The method is verified on a 4.4 kW prototype with a 150 mm air gap. Experimental results show that the target CC and CV charging profile can be achieved with up to 120 mm of lateral misalignment. When fully aligned, the maximum system conversion efficiency reaches 97.5%. It stays above 95.5% and 93.3% over the entire CC and CV mode ranges.**

***Index Terms*—Constant current (CC)/constant voltage (CV) charging, frequency tracking, inductive power transfer (IPT), misalignment tolerance, wireless power.**

Manuscript received July 6, 2021; revised November 24, 2021 and January 24, 2022; accepted March 12, 2022. Date of publication March 22, 2022; date of current version May 23, 2022. This work was supported by the National Natural Science Foundation of China under Grant 51977190. The work of Dehong Xu, Philip T. Krein, and Hao Ma was supported by the Zhejiang University/University of Illinois at Urbana-Champaign Institute. Recommended for publication by Associate Editor L. Zhang. *(Corresponding author: Hao Ma.)*

Zhuhaobo Zhang and Hao Ma are with the College of Electrical Engineering, Zhejiang University, Hangzhou 310027, China, and also with the Zhejiang University/University of Illinois at Urbana-Champaign Institute, Haining 314400, China (e-mail: zzhbpain@163.com; mahao@zju.edu.cn).

Shaoting Zheng, Shiying Luo, and Dehong Xu are with the College of Electrical Engineering, Zhejiang University, Hangzhou 310027, China (e-mail: 3150103536@zju.edu.cn; 11910041@zju.edu.cn; xdh@cee.zju.edu.cn).

Philip T. Krein is with the College of Electrical Engineering, Zhejiang University, Hangzhou 310027, China, with the Zhejiang University/University of Illinois at Urbana-Champaign Institute, Haining 314400, China, and also with the University of Illinois at Urbana-Champaign, Champaign, IL 61820 USA (e-mail: krein@illinois.edu).

Color versions of one or more figures in this article are available at https://doi.org/10.1109/TPEL.2022.3160497.

Digital Object Identifier 10.1109/TPEL.2022.3160497

I. Introduction

INDUCTIVE power transfer (IPT) technology has become a promising battery charging approach for commercial applications ranging from watts to multiple kilowatts. Bulky cables are avoided and galvanic isolation is achieved. This provides advantages of high convenience, high safety, and low maintenance [1]–[4].

This article builds on prior work with frequency adjustments in IPT systems, where constant current (CC) and constant voltage (CV) charging can be achieved when fully aligned. A multiband frequency tracking (MBFT) control is proposed to achieve efficient CC–CV charging and to mitigate misalignment. One frequency band supports CV mode and two separate bands support CC mode. When there is misalignment between transformer pads, target outputs can be tracked with a closed-loop adaptive frequency control while limiting input reactive power. The proposed method offers narrow operating frequency ranges, high misalignment tolerance, explicit design procedures, and high efficiency in both CC and CV modes.

Lithium batteries are usually charged with a CC interval followed by a CV interval [5]. This two-step method presents challenges for IPT chargers. Misalignment between the primary and secondary pads tends to decrease coupling and power transmission capability [6]. Various circuit topologies and control strategies have been proposed to mitigate misalignment impact on charging profiles. For example, an additional dc–dc stage can be added [7], [8]. The extra stage increases cost and tends to compromise efficiency. With a single-stage circuit structure, a compensation switching method used additional ac switches for reconfigurable CC and CV structures in [9], [10]. A cascaded hybrid structure was combined in [10] to enhance misalignment tolerance. At fixed operating frequencies, CC–CV and constant power battery charging were achieved with a variable inductor in [11] and a switched capacitor in [12]. Resonance was tracked with a closed-loop control.

Frequency adjustments are conventional for resonant converters. For IPT systems, frequency characteristics vary due to relatively low coupling. A pulse frequency modulation (PFM) method with a fixed duty ratio was employed in [13] and [14]. A wide frequency range was required to match varying load impedances. Deviations from the resonant point resulted in high

reactive power. The operating frequency range for zero-voltage switching (ZVS) was constrained by a phase-locked loop and a duty ratio control in [15]. The optimal range was further analyzed in [16]. Based on PFM, a frequency ride-through method was proposed to provide load-independent CC and CV outputs at two operating frequencies. Batteries could be charged without additional switches or circuit components. In [17] and [18], two separate frequencies were identified to match CC and CV modes based on series–series (S–S) compensation. The method was adapted to series–parallel (S–P) compensation in [19] and [20]. For these single capacitor compensation topologies, unity power factor conditions were met at only one load-independent frequency. In contrast, large inductive phase angles lead to high reactive power, high component stresses, and substantial power losses for other load-independent frequencies. The method was combined with an active rectifier in [21] to solve high reactive power issues. Higher order compensation topologies, such as *LCC-S* [22], *LCCC-S* [23], *LCL-LCL* [24], and *LCC-LCC* [25], were explored in fully aligned cases to obtain unity power factor for load-independent $f_{\rm CC}$ and $f_{\rm CV}$. Using similar strategies, an IPT system with two intermediate coils to improve coupling was discussed in [26]. In [27], *S-SP* compensation was selected with a minimum number of resonant components.

Frequency ride-through methods maintain frequencies in CC and CV modes as load impedance changes. In prior work, the methods have been limited by misalignment. Either $f_{\rm CC}$ or $f_{\rm CV}$ will lose resonance with misalignment. In this article, MBFT control is proposed to match CC and CV charging modes and to solve misalignment issues by actively adjusting the frequency. In CC mode, two narrow frequency bands near $f_{\rm CC}$ are selected to deliver target output currents and to limit reactive power. The inverter duty ratio controls target output voltages in CV mode. Compared to prior IPT methods, the proposed control inherits the advantages of frequency ride-through methods [22]–[27]. A dc–dc stage is avoided. CC and CV charging modes can be achieved with a single IPT stage without additional switches. When fully aligned, unity power factor can be obtained in both CC and CV modes. The proposed control adds at least three unique advantages. First, battery charging that tolerates high misalignment can be achieved. The approach effectively extends frequency ride-through methods to consider misalignment. Second, when there is misalignment, battery charging targets can be achieved with narrow operating frequency ranges and limited phase angles. This limits reactive power to avoid system efficiency penalties. Third, explicit design procedures can be presented for a series *LCC* topology. Parameter tuning designs are elaborated in the article.

The rest of the article is structured as follows. The circuit topology and modeling are analyzed in Section II. Constraints on CC and CV modes and relationships for $f_{\rm CC}$ and $f_{\rm CV}$ are shown. Based on the constraints, parameter design procedures are listed in Section III. The proposed MBFT control is elaborated in Section IV to obtain a highly efficient system. In Section V, experimental results are obtained from a 4.4 kW prototype to validate the proposed control. In Section VI, discussion and comparisons are given. Finally, Section VII concludes this article.

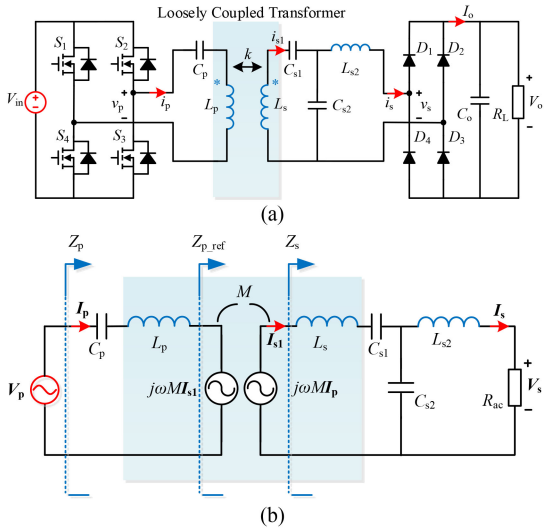

Fig. 1. (a) Circuit topology with series *LCC* compensation. (b) Equivalent mutual inductance circuit model.

II. Circuit Topology and Modeling

As shown in Fig. 1, a circuit topology with series *LCC* compensation was selected to implement the proposed control. A mutual inductance model for the loosely coupled transformer is represented by the shaded area. The primary circuit is composed of a full-bridge inverter and a transmitter coil with one compensation capacitor in series. The inverter consists of four power MOSFETs (S_1–S_4). The secondary circuit consists of a full-bridge rectifier (diodes D_1–D_4) and a receiver coil with *LCC* compensation. Inductances $L_{\rm p}$ and $L_{\rm s}$ correspond to the self-inductances of transmitter and receiver coils. Their mutual inductance and coupling coefficient are represented as M and k.

The fundamental harmonic approximation method [28] is used to analyze the circuit. Ignoring high-order harmonics, define

$$\begin{cases} V_{\rm p} = \frac{4}{\pi} V_{in}, V_{\rm s} = \frac{4}{\pi} V_{\rm o} \\ R_{\rm ac} = V_{\rm s}/\frac{\pi}{2} I_o = \frac{8}{\pi^2}\frac{V_{\rm o}}{I_o} = \frac{8}{\pi^2} R_{\rm L} \end{cases} \tag{1}$$

where $V_{\rm in}$ and $V_{\rm o}$ are the system input and output dc voltages, $V_{\rm p}$ and $V_{\rm s}$ are magnitudes of the fundamental harmonic voltages after the inverter and before the rectifier, respectively, and $R_{\rm L}$ and $R_{\rm ac}$ are the load and system equivalent load seen after and before the rectifier, respectively.

From Fig. 1(b), Kirchhoff's voltage law gives

$$\begin{cases} \dot{V}_{\rm p} = \dot{I}_{\rm p}\left(j\omega L_{\rm p} + \frac{1}{j\omega C_{\rm p}}\right) + j\omega M\ \dot{I}_{\rm s1} \\ j\omega M\ \dot{I}_{\rm p} = \dot{I}_{\rm s1}\left(j\omega L_{\rm s} - \frac{1}{j\omega C_{\rm s}}\right) + \frac{1}{j\omega C_{\rm s2}}(\dot{I}_{\rm s1} - \dot{I}_{\rm s}) \\ \dot{I}_{\rm s} R_{\rm ac} = j\omega L_{\rm s2}\dot{I}_1 + \frac{1}{j\omega C_{\rm s2}}(\dot{I}_{\rm s1} - \dot{I}_{\rm s}) \end{cases} \tag{2}$$

where ω represents the system frequency in rad/s. As shown in Fig. 1(b), $Z_{\rm p}$, $Z_{\rm p\_ref}$, and $Z_{\rm s}$ are equivalent impedances seen from various terminals of the circuit. Details for input impedance $Z_{\rm p}$ and for its phase angle are given in the Appendix. Parameters

Z_{p1}, Z_{s1}, and Z_{s2} can be represented as

$$\begin{cases} Z_{p1} = 1 - \omega^2 C_p L_p \\ Z_{s1} = 1 - \omega^2 C_{s2} L_{s1}, L_{s1} = L_s - \frac{1}{\omega^2 C_{s1}} \\ Z_{s2} = 1 - \omega^2 C_{s2} L_{s2}. \end{cases} \tag{3}$$

Conservation of energy requires

$$\mathbf{Re}\left[\dot{V}_p \overset{*}{I}_p\right] = \mathbf{Re}\left[\frac{\left(V_p/\sqrt{2}\right)^2}{Z_p}\right] = \frac{\left(\frac{V_s}{\sqrt{2}}\right)^2}{R_{ac}} = \frac{{V_o}^2}{R_L} \tag{4}$$

in the lossless case. The transconductance and voltage gain characteristics of the series *LCC* circuit, G_{CC} and G_{CV}, are

$$G_{CC} = \frac{I_o}{V_{in}} = \sqrt{\left(\frac{8}{\pi^2}\frac{1}{R_L}\right)\mathbf{Re}\left[\frac{1}{Z_p}\right]} = \sqrt{\left(\frac{8}{\pi^2}\right)^2 \frac{1}{R_{ac}}\mathbf{Re}\left[\frac{1}{Z_p}\right]} \tag{5}$$

$$G_{CV} = \frac{V_o}{V_{in}} = \sqrt{\left(\frac{8}{\pi^2}R_L\right)\mathbf{Re}\left[\frac{1}{Z_p}\right]} = \sqrt{R_{ac}\,\mathbf{Re}\left[\frac{1}{Z_p}\right]}. \tag{6}$$

The complicated expansions of G_{CC} and G_{CV} are provided in the Appendix. Constraints on load-independent CC and CV modes can be obtained.

A. Constraints on CC Mode When Fully Aligned

Battery charging usually starts in CC mode. Coefficients of load resistance R_{ac} in G_{CC} should be zero to support load-independent CC output. This requires

$$Z_{p1}Z_{s1} - (\omega^2 M^2)\omega^2 C_p C_{s2} = 0. \tag{7}$$

This constraint can be simplified to

$$M^2 = \left(\frac{1}{{\omega_{CC}}^2 C_p} - L_p\right)\left(\frac{1}{{\omega_{CC}}^2 C_{s2}} + \frac{1}{{\omega_{CC}}^2 C_{s1}} - L_s\right) \tag{8}$$

where ω_{CC} represents the system operating angular frequency for CC mode. Two implicit constraints from (7) are

$$\begin{cases} Z_{p1} = 1 - {\omega_{CC}}^2 C_p L_p \neq 0 \\ Z_{s1} = 1 - {\omega_{CC}}^2 C_{s2} L_{s1} \neq 0. \end{cases} \tag{9}$$

Unity power factor is important for an IPT charger when fully aligned. This requires

$$\arg(Z_p) = tan^{-1}(Z_p) = 0. \tag{10}$$

Based on (8) and (9), (10) can be simplified to give

$${\omega_{CC}}^2 + \frac{1}{{\omega_{CC}}^2 L_s L_{s2} C_{s2} C_{s1}} = \frac{1}{L_s C_{s2}} + \frac{1}{L_{s2} C_{s2}} + \frac{1}{L_s C_{s1}}. \tag{11}$$

In CC mode, (8) and (11) constitute circuit constraints on ω_{CC} in the fully aligned case.

B. Constraints on CV Mode When Fully Aligned

Charging power reaches its maximum at the end of CC mode. Current tapers off during the subsequent CV mode. The preceding analysis can be extended to load-independent CV output. The angular frequency transitions from ω_{CC} to ω_{CV}. The coefficients of load resistance in G_{CV} should be zero to ensure that load changes have no influence on the circuit voltage gain. This requires

$$Z_{p1}(\omega L_{s1} + \omega L_{s2} Z_{s1}) + (\omega^2 M^2)\omega C_p Z_{s2} = 0. \tag{12}$$

Similarly, we seek ω_{CV} to satisfy input unity power factor when fully aligned, which requires

$$\begin{cases} 1 - {\omega_{CV}}^2 C_p L_p = 0 \\ {\omega_{CV}}^2 L_s = \frac{1}{C_{s1}} + \frac{1}{C_{s2}} \\ 1 - {\omega_{CV}}^2 C_{s2} L_{s2} = 0. \end{cases} \tag{13}$$

In CV mode, (13) constitutes circuit constraints on ω_{CV} in the fully aligned case.

C. Constraint Relationships for ω_{CC} and ω_{CV}

In practice, resonant component values are fixed. The operating angular frequency stays near ω_{CC} in CC mode and near ω_{CV} in CV mode. Hence, parameter selection should follow constraints in CC and CV modes. From (8), (11), and (13), capacitance terms C_p, C_{s1}, and C_{s2} can be canceled. Two constraint relations for ω_{CC} and ω_{CV} are given by

$$\begin{cases} \left(\frac{\omega_{CC}}{\omega_{CV}}\right)^2 + \left(\frac{\omega_{CV}}{\omega_{CC}}\right)^2 \left(1 - \frac{L_{s2}}{L_s}\right) = 2 \\ \left(\frac{\omega_{CV}}{\omega_{CC}}\right)^4 = \frac{M^2}{L_p L_{s2}}. \end{cases} \tag{14}$$

This implies that

$$k^2\left(\frac{L_s}{L_{s2}}\right) - 2k\sqrt{\frac{L_s}{L_{s2}}} + (1 - k^2) = 0. \tag{15}$$

There are two sets of solutions for constraint relations (14) and (15)

$$\frac{L_s}{L_{s2}} = \left(\frac{1+k}{k}\right)^2 \Rightarrow \omega_{CC,1} = \frac{\omega_{CV}}{\sqrt{1+k}} \tag{16}$$

$$\frac{L_s}{L_{s2}} = \left(\frac{1-k}{k}\right)^2 \Rightarrow \omega_{CC,2} = \frac{\omega_{CV}}{\sqrt{1-k}} \tag{17}$$

where

$$k = \frac{M}{\sqrt{L_p L_{s1}}}. \tag{18}$$

The solutions show that $\omega_{CC,1}$ is less than ω_{CV} and $\omega_{CC,2}$ is greater than ω_{CV}. When fully aligned, values $\omega_{CC,1}$ and $\omega_{CC,2}$ correspond to capacitive and zero angles for the input impedance Z_p. The parameter ω_{CC} refers to $\omega_{CC,2}$ in the following discussion.

Based on (17), circuit transconductance at ω_{CC} and circuit voltage gain at ω_{CV} can be simplified as

$$G_{CC} = \frac{I_o}{V_{in}} = \frac{8}{\pi^2}\frac{1-k}{k}\frac{1}{\omega_{CC} M} \tag{19}$$

$$G_{CV} = \frac{V_o}{V_{in}} = \sqrt{\frac{L_{s1}}{{\omega_{CV}}^2 M^2 C_{s2}}} = \frac{L_{s1}}{M} = \frac{L_{s2}}{M}. \tag{20}$$

These are linked to resonant inductances L_p, L_{s1}, L_{s2}, and the maximum coupling coefficient k when fully aligned. In

TABLE I
IPT BATTERY CHARGER SPECIFICATIONS FOR THIS WORK

Parameters	Symbols	Values
Nominal power rating	P_o	4.4 kW
Input voltage	V_{in}	400 V
Output voltage	V_o	245-400 V
Charging current	I_o	1.1-11 A
Load resistance	R_L	22-364 Ω

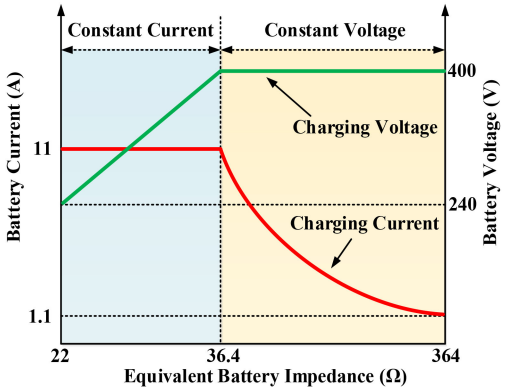

Fig. 2. Target CC and CV charging profile for 4.4 kW power rating.

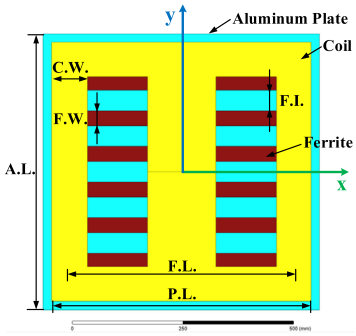

Fig. 3. Employed DD structure for the IPT battery charger.

practice, the input voltage and charging current and voltage are predetermined from battery specifications. Equations (19) and (20) provide constraints on circuit parameters at respective operating frequencies.

III. PARAMETER DESIGN PROCEDURES

Specifications of the IPT charger to be explored here are given in Table I. The nominal power and battery charging parameters match an actual IPT charger prototype for an electric vehicle. The target CC and CV charging profile is illustrated in Fig. 2. Initially, the charger delivers 11 A as the battery voltage increases. Charging power reaches a maximum at the 400 V battery voltage limit. Current tapers off during the subsequent CV mode. The process ends when the current drops to 1.1 A. The load impedance rises from 22 to 364 Ω.

The prototype here uses a DD pad structure like those explored in [29] and [30], and is shown in Fig. 3. The geometric parameters are given in Table II. Measured coupling coefficient k versus

TABLE II
SPECIFICATIONS OF THE PAD DIMENSIONS

Attributes	Symbols	Values
Ferrite length	F.L.	480 mm
Ferrite width	F.W.	40 mm
Ferrite interval	F.I.	47.5 mm
Coil width	C.W.	80 mm
Pad length	P.L.	600 mm
Aluminum length	A.L.	625 mm
Air gap	/	160 mm

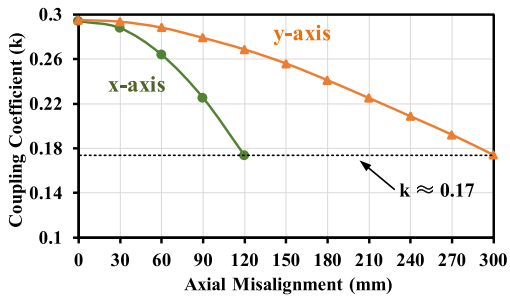

Fig. 4. Measured coupling coefficients for lateral (x-axis) and vertical (y-axis) misalignment.

axial misalignment is shown in Fig. 4. Misalignment perpendicular to the ferrite bars, in the y-direction, has less impact than x-axis misalignment. The misalignment range for design and test is selected to achieve at least 60% of the maximum coupling coefficient value. From Fig. 4, the allowed misalignment values in x and y directions can be as much as 120 and 300 mm, respectively.

From Table I and Fig. 4, system parameters $G_{\rm CC}$, $G_{\rm CV}$, and k are 0.0275, 1, and 0.29 at maximum coupling. Based on these values, the other nine circuit parameters can be determined step-by-step.

1) The system operating frequency for CV mode should be specified. In this design, $f_{\rm CV}$ is set to 105 kHz.
2) The system operating frequency for CC mode ($\omega_{\rm CC}$) can be determined from (17).
3) Based on the circuit transconductance in (19), M when fully aligned is

$$M = \frac{8}{\pi^2}\frac{1-k}{k}\frac{1}{\omega_{\rm CC}G_{\rm CC}}. \tag{21}$$

4) From (20), the secondary resonant inductance $L_{\rm s2}$ can be determined as

$$L_{\rm s2} = MG_{\rm CV}. \tag{22}$$

5) From (17), the secondary coil inductance $L_{\rm s}$ is

$$L_{\rm s} = L_{\rm s2}\left(\frac{1-k}{k}\right)^2. \tag{23}$$

6) Based on values of k, M, and $L_{\rm s}$, the primary coil inductance $L_{\rm p}$ can be determined from (18).
7) It is necessary to check whether the calculated coil inductances are feasible for transformer dimensions. If the results are satisfied, then resonant capacitances $C_{\rm p}$, $C_{\rm s1}$,

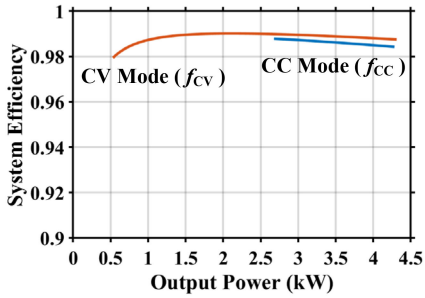

Fig. 5. Theoretical dc–dc conversion efficiency for various load resistances when fully aligned.

and C_{s2} can be determined from (13). Otherwise, ω_{CV} and pad dimensions need to be adjusted.

Circuit parameters can be determined uniquely with this process. System specifications in Table I are satisfied with two load-independent operating frequencies.

Series resistances of the transmitter and receiver coils influence system output and generate losses. The preceding analysis can be extended to include resistance, except that (4) is not applicable. Here, primary and secondary coil resistances are set to 0.3 Ω to estimate losses. When there is no misalignment, dc–dc conversion efficiency in CC and CV modes from the analysis is shown in Fig. 5 at f_{CC} and f_{CV}. From Fig. 5, the efficiency in CV mode is slightly higher than in CC mode at a given output power. This is because the secondary coil current at f_{CC} is higher than at f_{CV}. For example, at 4 kW output, primary coil currents are both 11.2 A. Secondary coil currents at f_{CC} and f_{CV} are 8.1 and 5.9 A. The efficiency difference is inherent to *S-LCC* compensation with circuit parameters set uniquely following steps 1)–7). Similar efficiency results were demonstrated in [22] and [23] with *LCC-S* and *LCCC-S* topologies.

IV. MBFT Control

In Fig. 6, frequency characteristics for various system charging currents and voltages and phase angles of impedance Z_p are demonstrated when there is alignment. There are two frequencies corresponding to unity power factor. Circuit voltage gain and transconductance stay constant over the load resistance range at these values. Conventional frequency ride-through methods select these frequencies to match target CC and CV modes when fully aligned, but use the same values when misalignment occurs.

In CC mode, parameter constraint (8) contains mutual inductance. This means that a circuit that uses the unity power factor frequency f_{CC} in Fig. 6 will lose resonance with misalignment. In contrast, parameter constraint (13) is not related to coupling in CV mode. Coupling coefficient variations in CV mode lead only to voltage gain variations, and resonance is unaffected. This leads to distinct strategies for the proposed MBFT control. In CV mode, (20) shows that output voltage increases when misalignment occurs. This can be compensated by adjusting the primary inverter duty ratio. The CV output can be maintained with fixed operating frequency f_{CV}, not altered by misalignment, although unity power factor might not be achieved unless aligned.

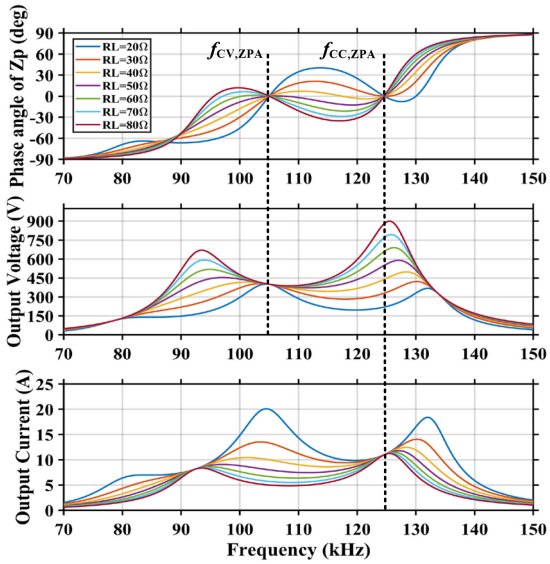

Fig. 6. System charging currents, charging voltages, and the phase angles of input impedance Z_p for various operating frequencies when there is alignment.

To consider the proposed MBFT control in CC mode, frequency characteristics for various system charging currents and phase angles of impedance Z_p are shown in Fig. 7, for aligned and misaligned cases. Three cases are selected to demonstrate three different control strategies. As shown in Fig. 7(a)–(c), operating frequencies deviate from the original f_{CC} point. Corresponding input phase angles become inductive. As shown in Fig. 7(d)–(f), the new frequencies can be taken as limits, with a high-frequency band (HFB) above nominal operation and a low-frequency band (LFB) below nominal operation. The operating frequency is adjusted within these bands to track the target charging current.

Misaligned case I shown in Fig. 7(a) and (d) corresponds to $k = 0.24$, a relatively high coupling condition. From Fig. 7(d), peak output currents in the HFB decrease as load resistance increases. The minimum current is higher than the target 11 A value. This means that the target CC-mode charging current can be achieved in HFB operation for various load resistances. In practice, intersection points on the left sides of the peaks are tracked. From Fig. 7(a), corresponding phase angles of Z_p are below 25°, ensuring relatively low reactive power.

Misaligned case II shown in Fig. 7(b) and (e) corresponds to $k = 0.21$, a medium coupling condition. From Fig. 7(e), the maximum and minimum current values in HFB operation are higher and lower than the target 11 A value. For load resistances between 25 and 27.5 Ω, the target charging current can be tracked in HFB operation. For higher load resistance values, operating frequencies should shift to the LFB. From Fig. 7(b), corresponding phase angles of impedance Z_p are approximately 35° for intersection points in both HFB and LFB operations, corresponding to 0.82 power factor.

Misaligned case III shown in Fig. 7(c) and (f) corresponds to $k = 0.19$, a relatively low coupling condition. From Fig. 7(f), the maximum current values in HFB operation are less than 11 A. The target charging current can be only achieved in LFB operation. From Fig. 7(c), corresponding phase angles

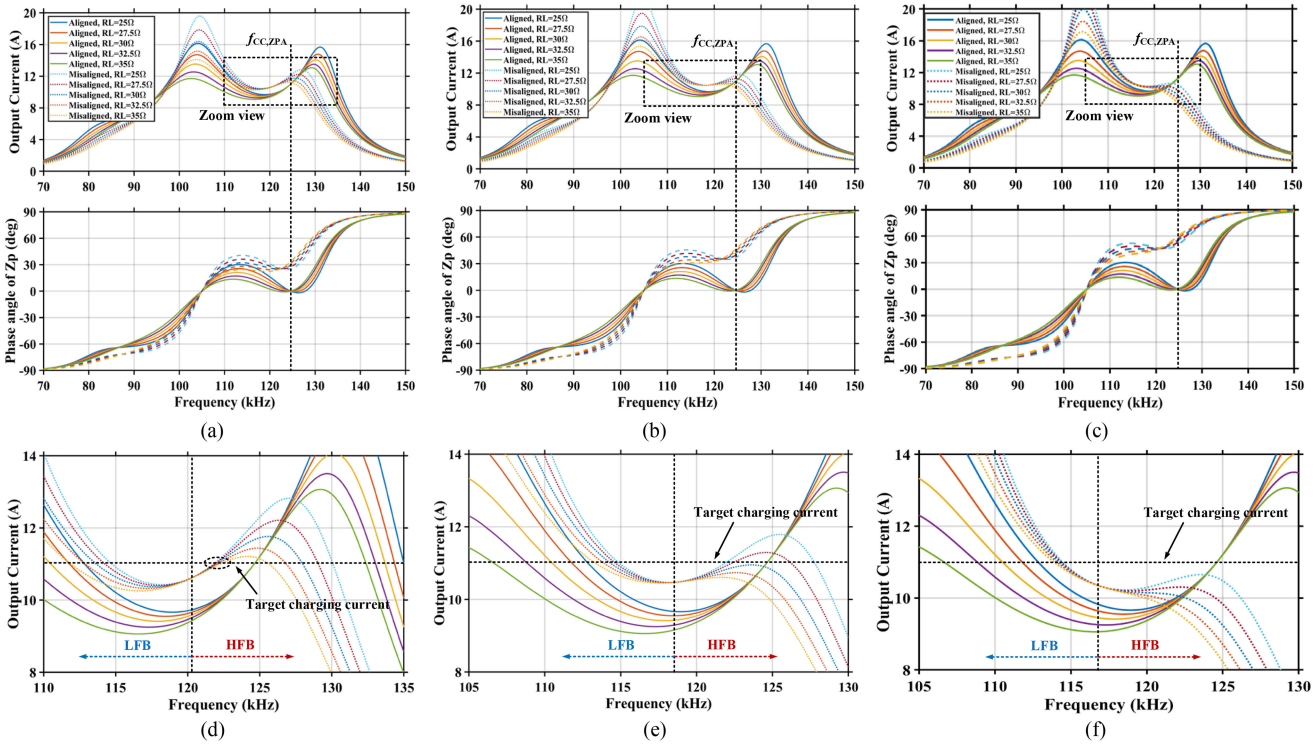

Fig. 7. System charging currents and the phase angles of input impedance Z_p for various operating frequencies. (a) For aligned case ($k = 0.29$) and misaligned case I ($k = 0.246$). (b) For aligned case ($k = 0.29$) and misaligned case II ($k = 0.217$). (c) For aligned case ($k = 0.29$) and misaligned case III ($k = 0.194$). (d) Zoom view of the case in (a). (e) Zoom view of the case in (b). (f) Zoom view of the case in (c).

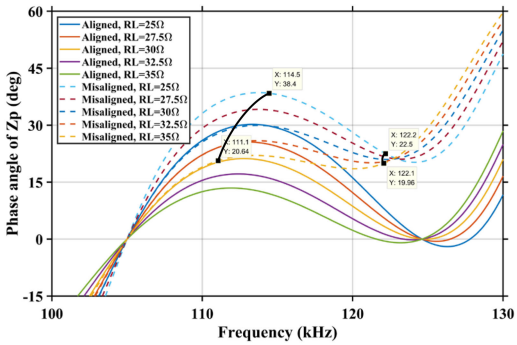

Fig. 8. Phase angles of input impedance Z_p for aligned case ($k = 0.29$) and misaligned case ($k = 0.25$) in CC mode.

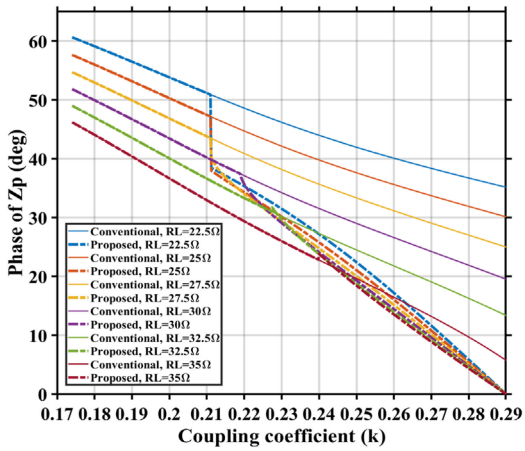

Fig. 9. Phase angles of input impedance Z_p for various misalignment and load resistance cases with conventional PFM and the proposed MBFT control method in CC mode.

of impedance Z_p are between 40° and 52°, corresponding to a minimum of 0.62 power factor. Although reactive power has grown, this is a relatively severe misalignment case, and a higher power factor would require reduced charge current.

It is worth noticing that the target charging current can be achieved in both HFB and LFB operations for a range of misalignment cases. Comparisons of phase angles of Z_p in HFB and LFB operations are shown for two cases in Fig. 8. In HFB operation, the frequency and phase angle ranges are 122.1–122.2 kHz and 20.0°–22.5° to achieve the target charging current. The LFB frequency and phase angle ranges are 111.1–114.5 kHz and 20.6°–38.4°. Typically, HFB operation is preferred if the target current can be reached since it requires less reactive power.

Conventional PFM methods operate over a frequency range with monotonic gain characteristics. From Fig. 7, the target charging current can be always achieved in LFB operation. This can represent a conventional PFM method. In CC mode, Fig. 9 compares phase angles of Z_p for various misalignment and load resistance cases between conventional PFM and the proposed MBFT control method. Dotted lines represent the proposed method and solid lines are the conventional approach. When coupling coefficient k exceeds 0.24, HFB operation requires much lower reactive power than LFB operation in CC mode.

TABLE III
CALCULATED FREQUENCY AND PHASE ANGLE RANGES

Coupling coefficient k	Frequency Ranges in CC mode	Phase angle ranges for Z_p
0.29 (100%)	124.6 kHz (HFB)	0°
0.276 (95%)	123.6 kHz - 123.7 kHz (HFB)	6.15° - 8.17°
0.261 (90%)	122.7 kHz - 122.8 kHz (HFB)	13.11° - 16.69°
0.247 (85%)	122.1 kHz - 122.2 kHz (HFB)	19.97° - 23.89°
0.232 (80%)	121.7 kHz - 122.8 kHz (HFB) 113.2 kHz - 114.3 kHz (LFB)	28.23° - 30.53° 25.01° - 27.52°
0.218 (75%)	121.9 kHz - 122.3 kHz (HFB) 113.7 kHz - 114.5 kHz (LFB)	35.12° - 36.02° 30.11° - 37.52°
0.203 (70%)	113.9 kHz - 114.6 kHz (LFB)	35.53° - 52.94°
0.189 (65%)	113.8 kHz - 114.3 kHz (LFB)	40.73° - 56.79°
0.174 (60%)	113.4 kHz - 113.7 kHz (LFB)	46.19° - 59.64°

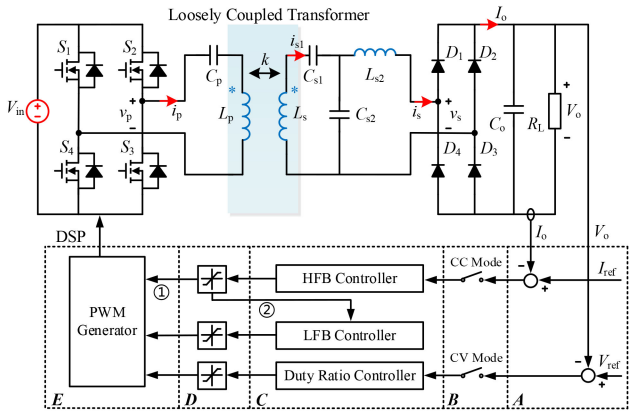

Fig. 10. Closed-loop control structure of the proposed MBFT method.

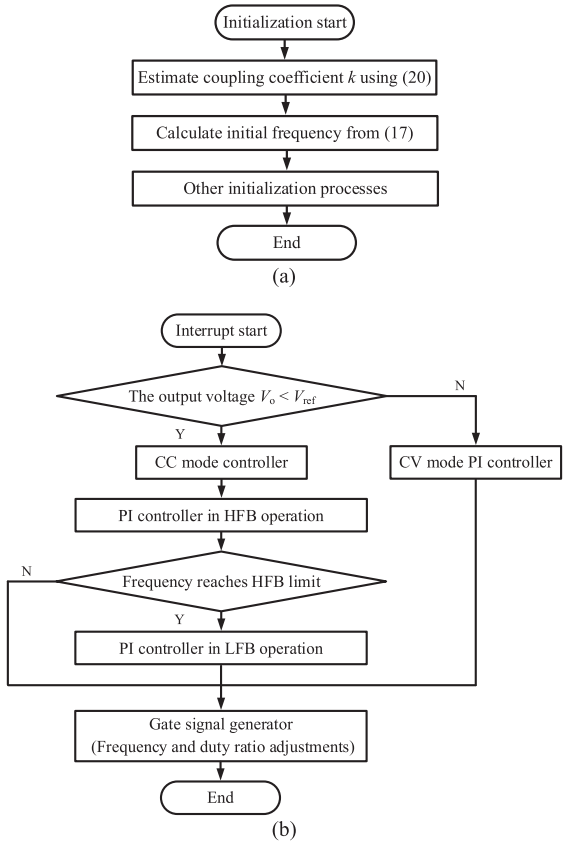

Fig. 11. Flowchart of the closed-loop control scheme. (a) Initialization. (b) Interrupt.

This corresponds to misaligned case I. When k is between 0.21 and 0.24, the system operates in the HFB at the beginning of CC mode, but shifts to the LFB above a certain output voltage. This corresponds to misaligned case II. When k is less than 0.21, the target charging current can be delivered only in LFB operation. This corresponds to misaligned case III. Typical frequency ranges and corresponding phase angles for several coupling cases have been calculated and are listed in Table III. The operating frequency ranges are narrow and phase angle changes are limited. From Table III and Fig. 9, these narrow frequency ranges and relatively low reactive power are important advantages of the proposed MBFT control method.

A suitable closed-loop structure for MBFT control is shown in Fig. 10 and a flowchart is shown in Fig. 11. The controller is implemented in a DSP, and is composed of parts *A*–*E* that represent error generation, mode selection, proportional integral (PI) controllers, PI limiters, and gate signal generation. Circuit output voltage and current should be sampled to allow the controller to compensate for misalignment and load variations. Coupling coefficient k can be estimated from (20). It can be measured during a preactivation process (i.e., zero current charging) at the designated f_{CV}. For battery charging, when the output voltage V_{o} is less than V_{ref}, the CC mode PI controller is activated. The initial operating frequency is set based on (17) and acts as the control boundary between HFB and LFB. The frequency is first adjusted upward with a PI controller for HFB operation. If the target output current is reachable, CC mode can be started. The frequency should return to the initial point if it reaches the HFB upper limit. This limit can be enforced by a PI limiter. If this occurs, the frequency is then adjusted downward with a separate PI controller for LFB operation. There is an LFB lower limit to prevent the IPT system from operating at undesirable frequencies. Once the output voltage V_{o} reaches V_{ref}, the system switches to CV mode. In CV mode, the duty ratio of the primary inverter can be adjusted with a voltage-based PI controller and the operating frequency is fixed at f_{CV}.

From Fig. 7, HFB upper limits are set to the frequencies at which peak output currents occur, subject to rating limits. Transconductance gain characteristics in HFB operation are monotonic. The limits help to avoid frequency bifurcation and to ensure control stability. They are linked to both load resistance R_{L} and coupling coefficient k. The limits can be calculated by setting the derivative of the charging current to zero, as in

$$\frac{dI_{\mathrm{o}}}{d\omega} = \frac{dV_{\mathrm{in}}G_{\mathrm{CC}}}{d\omega} = \frac{d}{d\omega}\left[V_{\mathrm{in}}\sqrt{\left(\frac{8}{\pi^2}\right)^2\frac{1}{R_{\mathrm{ac}}}\mathbf{Re}\left[\frac{1}{Z_{\mathrm{p}}}\right]}\right] = 0. \tag{24}$$

Calculated HFB limit frequencies for various misalignment and load resistance cases in CC mode are shown in Fig. 12. For cases with low coupling coefficients and high load resistances, the derivative (24) has no solution. This means that there is no

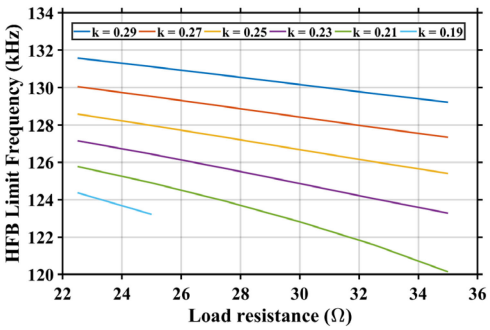

Fig. 12. HFB upper limit frequencies for various misalignment and load resistance cases in CC mode.

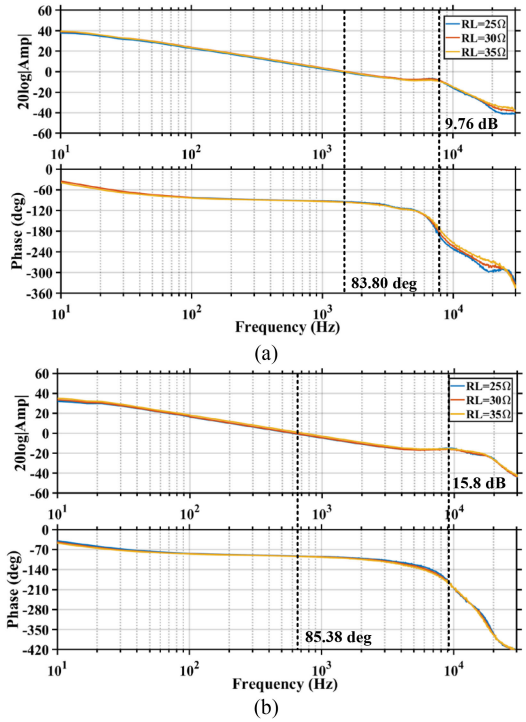

Fig. 13. Bode plots of the open-loop converter for various load resistances. (a) Steady-state operating frequency and coupling coefficient k are 113 kHz and 0.29. (b) Steady-state operating frequency and coupling coefficient k are 124 kHz and 0.18.

frequency bifurcation. The output current decreases monotonically, as shown in Fig. 7(f). For these cases, HFB limits can be set to a fixed value, such as 125 kHz in this design. In practice, limits can be saved in a look-up table. Considering practical component tolerances, the limits should be set slightly lower than given ideally in (24) to ensure control stability.

From Fig. 7, the target output current can be reached at only one frequency in LFB. There is no frequency bifurcation. This ensures control stability in LFB operation. The LFB lower limit frequency can be set to a fixed value, 112 kHz in this design, based on system current tolerance. This provides a method for resonant current protection in CC mode to deal with excessive misalignment. With these limits, HFB and LFB ranges for various cases can be determined.

In a practical vehicle charging application, the MBFT control is implemented when the vehicle is parked and communications between the vehicle and charging station have been established. The parameter k is expected to be fixed throughout the battery charging process. If the vehicle moves during charging, LFB operation cannot return to the HFB automatically. In practice, the MBFT control should be restarted as in Fig. 11 if the vehicle position changes.

To design PI controllers for HFB and LFB operations, control-to-output transfer functions need to be derived. Small-signal models of high-order resonant converters based on the extended describing function method [31], [32] are complicated. Instead, the ac sweep function in PSIM software was employed to draw Bode plots of control-to-output-current transfer functions. Open-loop characteristics for various load resistances are shown in Fig. 13. Steady-state operating frequencies of 113 and 124 kHz represent narrow LFB and HFB operation. Magnitude and phase margins are labeled in Fig. 13. The values ensure control stability. One set of PI parameters was employed for both LFB and HFB operation. Parameters k_{p} and k_{i} were selected as 1300 and 8.75×10^6.

In practice, the primary resonant capacitor C_{p} is selected to be about 5% higher than the designed value to provide a slightly inductive phase angle for Z_{p}, as in [33] and [34]. This supports ZVS operation of the primary inverter. The MOSFET turn-OFF current I_{OFF} is a crucial parameter for ZVS. I_{OFF} should be high enough to charge and discharge parasitic MOSFET output capacitance C_{oss}. The minimum I_{OFF} limit, from [35], is

$$I_{\mathrm{OFF}} > \frac{2C_{\mathrm{oss}}V_{\mathrm{in(max)}}}{t_{\mathrm{dead}}} \tag{25}$$

where $V_{\mathrm{in(max)}}$ represents the maximum input voltage and t_{dead} represents the inverter dead time. The calculated I_{OFF} limit is 1 A based on the C_{oss} value of the SiC MOSFET used here. From the expression of input impedance Z_{p} and Fig. 9, the worst case for I_{OFF} value in CC mode occurs at the minimum 22 Ω load resistance when fully aligned. If (25) can be satisfied for this case, ZVS operation can be ensured throughout the CC mode.

It should be noted that the primary inverter will lose ZVS operation in CV mode. This is because the inverter duty ratio is adjusted and unity power factor can be maintained at f_{CV}. In CV mode, the output power decreases gradually. Loss of ZVS has limited impact on system efficiency if it occurs at a low enough output power. A primary current limit needs to be enforced to deal with excessive misalignment, but the system should be activated only when misalignment lies within the design limits.

V. Experimental Results

A 4.4-kW IPT charging system prototype with series *LCC* compensation was built and tested to demonstrate the feasibility of the design parameters and the proposed MBFT control. The experimental prototype is shown in Fig. 14. The transformer pads match dimensions in Table II and measured parameters of components are listed in Table IV. The IPT system consisted of an H-bridge inverter, primary and secondary DD pads with

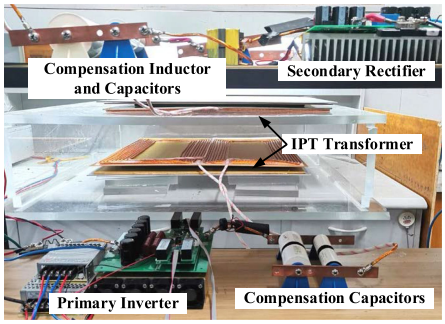

Fig. 14. 4.4-kW IPT experimental prototype.

TABLE IV
MEASURED RESONANT TANK PARAMETERS

Parameters	Symbols	Values
Transmitter coil inductance	L_{p1}	181.6 μH
Receiver coil inductance	L_s	554.5 μH
Primary resonant capacitance	C_p	13.39 nF
Secondary resonant capacitance	C_{s1}	5.08 nF
	C_{s2}	24.53 nF
Secondary resonant inductance	L_{s2}	92.76 μH
Resonant frequency for CV mode	f_{CV}	105 kHz
Resonant frequency for CC mode	f_{CC}	124 kHz

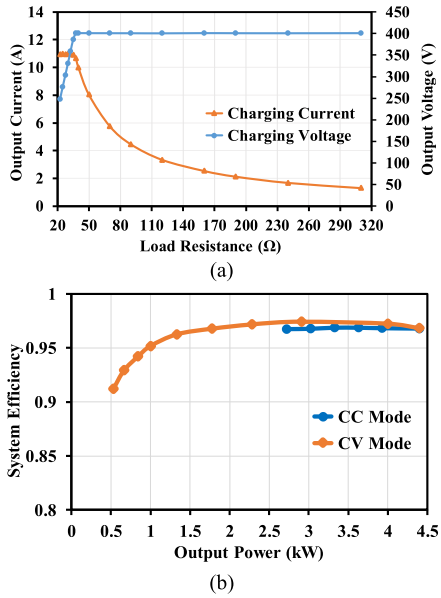

Fig. 15. (a) System output characteristics and (b) dc–dc conversion efficiency for various load resistances.

their compensation components, a diode rectifier bridge, and load resistances. A Chroma dc source (62100H-450) provided the input power. An electronic load (IT8096) was used to emulate lithium battery charging. The load's constant resistance (CR) mode was employed to validate the effectiveness of the MBFT control. CV and CC modes were used to ensure that the control can adapt to a real battery charging process. An SiC MOSFET module (SK45MH120TSCp) from Semikron was used for the full-bridge inverter and SiC Schottky diodes were used for the rectifier. Resonant inductors used PQ 50/50 ferrite cores. Polypropylene film capacitors in series and parallel combinations were used as compensation components. The system controller was implemented with a Texas Instruments TMS320F28335 DSP to generate precise inverter switching signals for frequency adjustments.

Experimental results for a CC and CV charging profile without misalignment are shown in Fig. 15(a). The electronic load is operated in CR mode. The charging currents and voltages track the commanded charging profile. The operating frequency range in CC mode was 122.6–123.2 kHz. The operating frequency in CV mode was fixed at 103 kHz. Comparing the ranges with theoretical frequency curves shown in Table III, the deviation is below 2%. Minor differences are due to adjustments of C_p for ZVS operation.

Experimental results for dc–dc conversion efficiency given various load resistances are shown in Fig. 15(b). The efficiency characteristics are in accordance with theoretical results in Fig. 5. The efficiency was 96.7% and 96.8% for CC and CV modes at full output power. It stayed above 96.6% throughout the CC mode and above 91.2% throughout the CV mode. Maximum system efficiency reached 97.5%, for 55 Ω load resistance. The efficiency dropped to 91.2% when charging power fell to 550 W in CV mode. The maximum efficiency gap between CC and CV modes is 0.6% for identical output power values.

Experimental waveforms for the IPT system are shown in Fig. 16 for loads of 27.5 and 90 Ω. The gate–source voltage v_{gs} for one MOSFET is shown, and v_p is the primary inverter output voltage. i_p and i_s represent primary and secondary resonant currents. i_o and v_o are system charging current and voltage. The respective operating frequencies and phase angles between v_{ds} and i_p are shown. Fig. 16(a) confirms that soft-switching conditions are met. In principle, unity power factor can be achieved in CV mode with the right choice of f_{CV}. In practice, the output voltage will increase by 10% at light load conditions in open-loop operation due to parasitic resistances and the increased value of C_p. For the MBFT control, the duty ratio was adjusted to track the target charging voltage and ZVS conditions were not met. When the load resistances were 27.5 and 90 Ω, the primary phase lags were 11° and 26°, corresponding to power factors of 0.98 and 0.9.

For misaligned cases, experimental results of system output current, output voltage, dc–dc system efficiency, and operating frequency for various lateral misalignment and load resistance cases are shown in Fig. 17. Full rated 11 A and 400 V outputs were respective CC and CV mode references. In Fig 17(a), (b), and (d), load resistances are shown on log scales given the wide range in CV mode. The maximum lateral misalignment of 120 mm was determined based on system current tolerance. From the MOSFET ratings, the allowable minimum coupling coefficient k_{min} can be calculated from (4) and Fig. 9 at the nominal 4.4 kW output power. A lower coupling coefficient leads to a higher reactive power and a higher resonant current. In terms of k_{min} and dimensions of the employed IPT pad structure, the maximum misalignment range can be determined as in Fig. 4.

From Fig. 17(c) and (d), maximum measured CC and CV mode efficiencies were 96.7% and 97.5%. The minimum CC

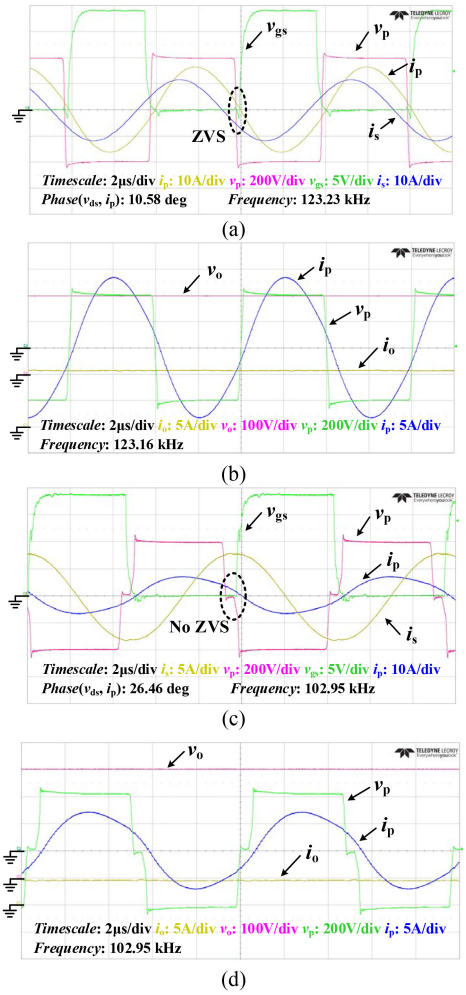

Fig. 16. Experimental waveforms of the IPT system when fully aligned. (a), (b) In CC mode ($R_L = 27.5\ \Omega$). (c), (d) In CV mode ($R_L = 90\ \Omega$).

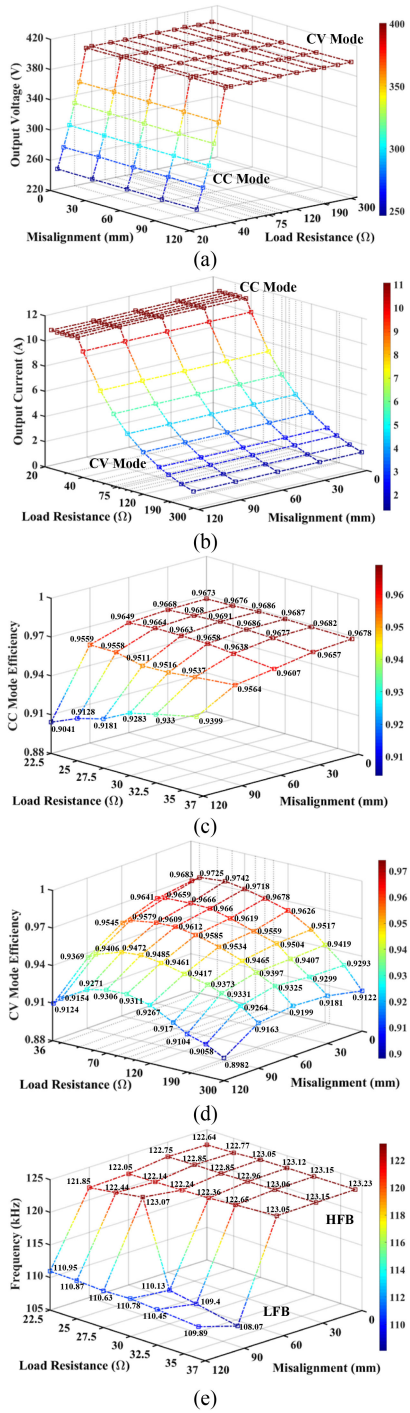

Fig. 17. Experimental results of (a) output current, (b) output voltage, (c) system efficiency in CC mode, (d) system efficiency in CV mode, and (e) system operating frequency in CC mode for various lateral misalignment and load resistance cases.

mode efficiency was 90.4%. This occurred at the lowest CC mode voltage and maximum misalignment. The minimum CV mode efficiency was 89.8%. This occurred at the lowest CV mode current and maximum misalignment. From Fig. 17(e), the operating frequency changed from HFB to LFB operation for low coupling coefficients and high load resistances. When misalignment was below 60 mm, the coupling coefficient k was above 0.263 and the target output current could be tracked in HFB operation. When misalignment was 90 mm, k was 0.225 and the operating frequency changed from HFB to LFB operation during charging. When misalignment was 120 mm, k was 0.173 and the target 11 A output could be tracked only in LFB operation. These coincide with the MBFT control results shown in Fig. 7. In CV mode, the operating frequency was fixed at 103 kHz and is not shown in Fig. 17(e).

Fig. 18 shows time-domain waveforms for misaligned cases. The load resistance was 27.5 Ω in CC mode and 90 Ω in CV mode. Soft-switching conditions were met in CC mode.

Experimental transient operation is explored in Fig. 19 with 90 mm misalignment. In Fig. 19(a), the CR load was switched between 22 and 27 Ω. The target output current could be tracked in HFB operation. In Fig. 19(b), the CR load was switched between 28 and 35 Ω. The target 11 A could be tracked in LFB operation. In Fig. 19(c), the CR load was switched between 25 and 35 Ω. A zoomed view is shown in Fig. 19(c), demonstrating the transition from HFB to LFB operation. The operating frequency was first adjusted upward. When the frequency reached the HFB upper limit for a predetermined interval, operation returned to the initial point and then was adjusted downward

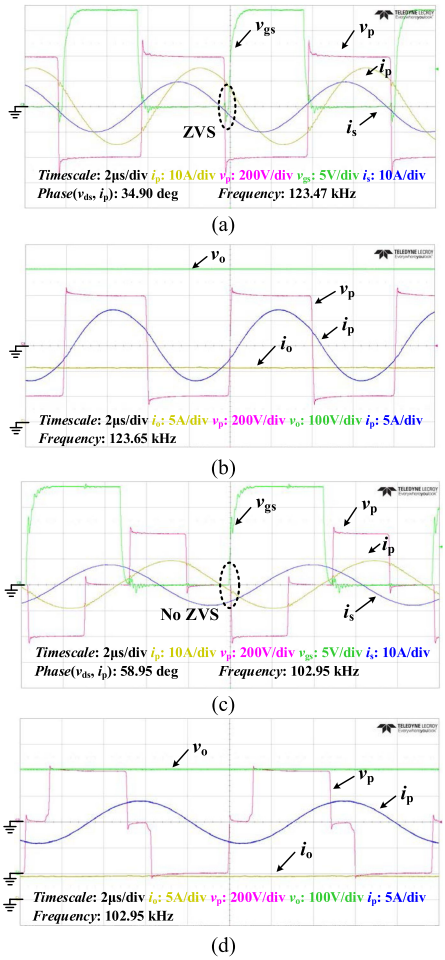

Fig. 18. Experimental waveforms of the IPT system with a 90 mm misalignment. (a), (b) In CC mode (R_L = 27.5 Ω). (c), (d) In CV mode (R_L = 90 Ω).

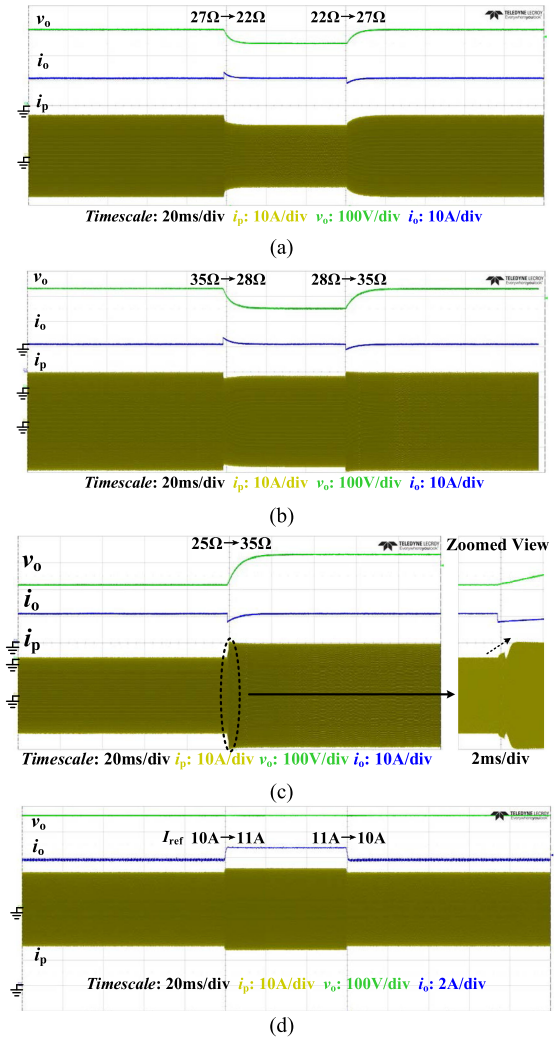

Fig. 19. Experimental transient waveforms of the IPT system with 90 mm misalignment. (a) In HFB operation with CR mode. (b) In LFB operation with CR mode. (c) From HFB to LFB operation with CR mode. (d) In HFB operation with CV mode.

for LFB operation. The zoomed view uses a 2 ms/div timescale. It can be seen that the output current increased as the control probed the HFB upper limit, but falls short of the target 11 A, triggering the band shifting process. In the end, the target current could be tracked in LFB operation. This process coincides with the MBFT control shown in Fig. 11. In Fig. 19(d), transient characteristics were explored with a CV load. In this case, the reference current switched between 10 and 11 A with a fixed 360 V load. It should be noted that the output current ripple is as low as 0.4% with a CR load. It increases to 2% with a CV load.

VI. Discussion and Comparisons

The MBFT control is proposed for misalignment tolerance. When fully aligned, two load-independent frequencies f_{CC} and f_{CV} are used for respective CC and CV outputs. When there is misalignment, the frequency is adjusted in two bands when in CC mode. The inverter duty ratio is adjusted in CV mode. If inverter duty ratio is selected as the control variable in CC mode, there will be three disadvantages. First, from Fig. 7, the output current at nominal f_{CC} decreases with misalignment. The inverter duty ratio should be highest when fully aligned and should decrease with misalignment to increase current gain. This is not a good approach because power utilization is limited and system efficiency will be affected. Second, ZVS will be lost during at least part of CC mode. ZVS in CC mode is important for efficiency. Third, resonance cannot be optimized, as in Fig. 9. High reactive power increases circuit losses.

If frequency is selected as the control variable in CV mode, the required system voltage gain cannot always be achieved. System output voltages and the input phase angles for various operating frequencies in CV mode are shown in Fig. 20. Voltage gain at frequency f_{CV} increases with misalignment. For low load resistances, f_{CV} operation provides a peak voltage gain point. For high load resistances, f_{CV} becomes a valley voltage gain point. The target voltage gain cannot be achieved since the frequency behavior bifurcates.

Table V reviews and compares a variety of resonant circuit compensation topologies, representing more conventional approaches to IPT control. Passive component count for each topology is also listed. Unity power factor conditions can be met at only one load-independent frequency for single capacitor

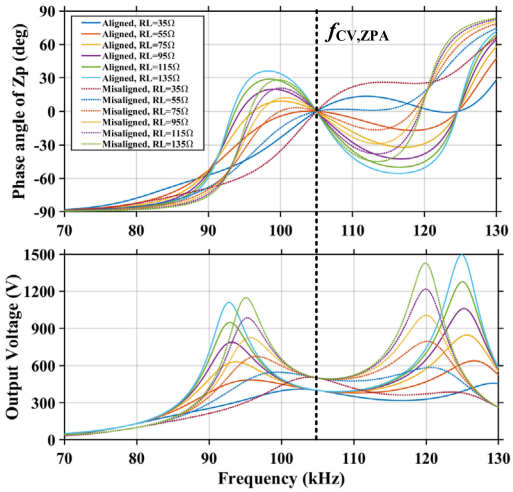

Fig. 20. System output voltages and the phase angles of input impedance Z_p for various operating frequencies in CV mode.

TABLE V
COMPARISONS OF RESONANT CIRCUIT COMPENSATION TOPOLOGIES

Topologies	Passive Component Count	Unity-power CC mode	Unity-power CV mode
S-S	2	Yes (↑)	No
S-P	2	No	Yes (↑)
P-S	2	No	Yes (↓)
P-P	2	Yes (↓)	No
S-SP	4 (1 dc inductor)	Yes (↓)	Yes (↑)
S-LCC	4	Yes (↓)	Yes (↑)
LCC-S	4	Yes (↓)	Yes (↓)

Note: ↑ refers to the case where the current/voltage gain increases with misalignment. ↓ refers to the case where the current/voltage gain decreases with misalignment.

compensation topologies *S-S*, *S-P*, *P-S*, and *P-P*. Large inductive phase angles lead to high reactive power and high power losses for other load-independent frequencies. Compared to the selected *S-LCC* topology, *S-SP* and *LCC-S* have the same passive component counts and similar characteristics. Resonance of their f_{CV} points is not affected by misalignment. For the *S-SP* topology, a dc filter inductor is needed in series with the rectifier. The filter inductor does not participate in resonance. High harmonic distortion before the rectifier will cause substantial errors with the fundamental harmonic approximation, especially for light loads. This complicates parameter design procedures and increases device stress [36]. For the *LCC-S* topology, MBFT control is unsuitable in CV mode. System voltage gain decreases with misalignment at f_{CV}. The inverter duty ratio should be adjusted to provide higher voltage gain. The approach limits power utilization and system efficiency. From these comparisons, the *S-LCC* topology is the best fit for MBFT control. Higher order compensation approaches such as *LCC-LCC* [25] have six compensation components and multiple load-independent f_{CC} and f_{CV} values. MBFT control has possibilities in these contexts, although implementation will be more complicated. This is an opportunity for further research.

The PFM method with variable duty ratio was employed in [15] to adjust voltage gain. In [15], a CV output is achieved with an *S-S* compensation topology. The operating frequency is adjusted monotonically above f_{CV} to compensate for misalignment. The inverter duty ratio is adjusted to set the input phase angle. From Table V, unity power factor cannot be achieved at f_{CV} with an *S-S* topology. Reactive power is relatively high. Compared to [15], the work in this article achieves target CC–CV output with the MBFT control and both f_{CC} and f_{CV} provide unity power factor points. Frequency control is used in CC mode and inverter duty ratio control is employed in CV mode. Compared to conventional PFM methods, the operating frequency ranges of the proposed MBFT control are narrow and phase angle changes are limited. These characteristics provide relatively low reactive power and are major advantages.

VII. CONCLUSION

In this article, an MBFT control for an IPT battery charger is proposed to achieve rated output in CC and CV modes even with substantial misalignment. Based on load-independent operating frequencies for CC and CV outputs, two narrow frequency bands are employed to compensate for misalignment while limiting reactive power. A 4.4 kW prototype was implemented and demonstrated the control strategy. Experimental results show that the proposed control supports high system efficiency with relatively narrow operating frequency ranges. The sample charging profile was achieved with up to 120 mm of lateral misalignment. Peak efficiency was 97.5% with a 150 mm air gap when fully aligned. Efficiency stayed above 95.5% and 93.3% throughout the CC and CV modes when aligned.

APPENDIX

Z_p is the equivalent impedance seen after the primary inverter. It can be derived from Fig. 1(b). Detail for Z_p and for its phase angle is given in (26) and (27). shown at the bottom of this page

$$Z_p = j\omega L_p + \frac{1}{j\omega C_p} + (\omega^2 M^2)\frac{1 + j\omega C_{s2}(R_{ac} + j\omega L_{s2})}{R_{ac} + j\omega(L_s + L_{s2}) + \frac{1}{j\omega C_{s1}} - \omega^2 L_{s1} C_{s2}(R_{ac} + j\omega L_{s2})}$$
$$= \frac{[Z_{p1} Z_{s1} R_{ac} - (\omega^2 M^2)\omega^2 C_p C_{s2} R_{ac}] + j[\omega L_{s1} Z_{p1} + \omega L_{s2} Z_{p1} Z_{s1} + (\omega^2 M^2)\omega C_p Z_{s2}]}{(-\omega^2 C_p)(L_{s1} + L_{s2} Z_{s1}) + j\omega C_p R_{ac} Z_{s1}} \quad (26)$$

$$\tan^{-1}(Z_p)$$
$$= \frac{[Z_{p1}(\omega L_{s1} + \omega L_{s2} Z_{s1}) + (\omega^2 M^2)\omega C_p Z_{s2}](-\omega^2 C_p)(L_{s1} + L_{s2} Z_{s1}) - \omega C_p R_{ac} Z_{s1}[Z_{p1} Z_{s1} R_{ac} - (\omega^2 M^2)\omega^2 C_p C_{s2} R_{ac}]}{[Z_{p1} Z_{s1} R_{ac} - (\omega^2 M^2)\omega^2 C_p C_{s2} R_{ac}](-\omega^2 C_p)(L_{s1} + L_{s2} Z_{s1}) + \omega C_p R_{ac} Z_{s1}[\omega L_{s1} Z_{p1} + \omega L_{s2} Z_{s1} Z_{p1} + (\omega^2 M^2)\omega C_p Z_{s2}]} \quad (27)$$

$$G_{\mathrm{CC}} = \frac{I_{\mathrm{o}}}{V_{\mathrm{in}}} = \sqrt{\left(\frac{8}{\pi^2}\right)^2 \frac{(-\omega^2 C_{\mathrm{p}})(L_{\mathrm{s1}} + L_{\mathrm{s2}} Z_{\mathrm{s1}})[Z_{\mathrm{p1}} Z_{\mathrm{s1}} - (\omega^2 M^2)\omega^2 C_{\mathrm{p}} C_{\mathrm{s2}}] + (\omega C_{\mathrm{p}} Z_{\mathrm{s1}})[Z_{\mathrm{p1}}(\omega L_{\mathrm{s1}} + \omega L_{\mathrm{s2}} Z_{\mathrm{s1}}) + (\omega^2 M^2)\omega C_{\mathrm{p}} Z_{\mathrm{s2}}]}{[Z_{\mathrm{p1}} Z_{\mathrm{s1}} - (\omega^2 M^2)\omega^2 C_{\mathrm{p}} C_{\mathrm{s2}}]^2 \boldsymbol{R_{\mathrm{ac}}}^2 + [Z_{\mathrm{p1}}(\omega L_{\mathrm{s1}} + \omega L_{\mathrm{s2}} Z_{\mathrm{s1}}) + \omega C_{\mathrm{p}}(\omega^2 M^2) Z_{\mathrm{s2}}]^2}} \tag{28}$$

$$G_{\mathrm{CV}} = \frac{V_{\mathrm{o}}}{V_{\mathrm{in}}} = \sqrt{\frac{(-\omega^2 C_{\mathrm{p}})(L_{\mathrm{s1}} + L_{\mathrm{s2}} Z_{\mathrm{s1}})[Z_{\mathrm{p1}} Z_{\mathrm{s1}} - (\omega^2 M^2)\omega^2 C_{\mathrm{p}} C_{\mathrm{s2}}] + (\omega C_{\mathrm{p}} Z_{\mathrm{s1}})[Z_{\mathrm{p1}}(\omega L_{\mathrm{s1}} + \omega L_{\mathrm{s2}} Z_{\mathrm{s1}}) + (\omega^2 M^2)\omega C_{\mathrm{p}} Z_{\mathrm{s2}}]}{[Z_{\mathrm{p1}} Z_{\mathrm{s1}} - (\omega^2 M^2)\omega^2 C_{\mathrm{p}} C_{\mathrm{s2}}]^2 + \left[\frac{Z_{\mathrm{p1}}(\omega L_{\mathrm{s1}} + \omega L_{\mathrm{s2}} Z_{\mathrm{s1}}) + (\omega^2 M^2)\omega C_{\mathrm{p}} Z_{\mathrm{s2}}}{\boldsymbol{R_{\mathrm{ac}}}}\right]^2}}. \tag{29}$$

These lead to complicated expressions of transconductance G_{CC} and voltage gain G_{CV}, which are given in (28) and (29). shown at the top of this page The load resistance terms are emphasized in boldface text. Coefficients of load resistance R_{ac} in G_{CC} or G_{CV} should be zero to support load-independent CC or CV output

REFERENCES

[1] G. A. Covic and J. T. Boys, "Inductive power transfer," *Proc. IEEE*, vol. 101, no. 6, pp. 1276–1289, Jun. 2013.

[2] S. Li and C. C. Mi, "Wireless power transfer for electric vehicle applications," *IEEE J. Emerg. Sel. Topics Power Electron.*, vol. 3, no. 1, pp. 4–17, Mar. 2015.

[3] W. X. Zhong and S. Y. R. Hui, "Maximum energy efficiency tracking for wireless power transfer systems," *IEEE Trans. Power Electron.*, vol. 30, no. 7, pp. 4025–4034, Jul. 2015.

[4] D. Patil, M. K. McDonough, J. M. Miller, B. Fahimi, and P. T. Balsara, "Wireless power transfer for vehicular applications: Overview and challenges," *IEEE Trans. Transp. Electrific.*, vol. 4, no. 1, pp. 3–37, Mar. 2018.

[5] D. Andrea, *Battery Management Systems for Large Lithium-Ion Battery Packs*, 1st ed. Boston, MA, USA: Artech House, 2010.

[6] C. S. Wang, O. H. Stielau, and G. A. Covic, "Design considerations for a contactless electric vehicle battery charger," *IEEE Trans. Ind. Electron.*, vol. 52, no. 5, pp. 1308–1314, Oct. 2005.

[7] M. Kim, D. Joo, and B. K. Lee, "Design and control of inductively power transfer system for electric vehicles considering wide variation of output voltage and coupling coefficient," *IEEE Trans. Power Electron.*, vol. 34, no. 2, pp. 1197–1208, Feb. 2019.

[8] R. Bosshard, J. W. Kolar, and B. Wunsch, "Control method for inductive power transfer with high partial-load efficiency and resonance tracking," in *Proc. IEEE Int. Power Electron. Conf*., May 2014, pp. 2167–2174.

[9] X. Qu, H. Han, S. Wong, C. K. Tse, and W. Chen, "Hybrid IPT topologies with constant current or constant voltage output for battery charging applications," *IEEE Trans. Power Electron.*, vol. 30, no. 11, pp. 6329–6337, Nov. 2015.

[10] Y. Chen, B. Yang, Z. H. Kou, Z. He, G. Cao, and R. Mai, "Hybrid and reconfigurable IPT systems with high-misalignment tolerance for constant current and constant voltage battery charging," *IEEE Trans. Power Electron.*, vol. 33, no. 10, pp. 8259–8269, Oct. 2018.

[11] Z. Zhang, F. Zhu, D. Xu, P. T. Krein, and H. Ma, "An integrated inductive power transfer system design with a variable inductor for misalignment tolerance and battery charging applications," *IEEE Trans. Power Electron.*, vol. 35, no. 11, pp. 11544–11556, Nov. 2020.

[12] Z. Huang, C. Lam, P. Mak, R. P. d. S. Martins, S. Wong, and C. K. Tse, "A single-stage inductive-power-transfer converter for constant-power and maximum-efficiency battery charging," *IEEE Trans. Power Electron.*, vol. 35, no. 9, pp. 8973–8984, Sep. 2020.

[13] C. Zheng *et al.*, "High-efficiency contactless power transfer system for electric vehicle battery charging application," *IEEE J. Emerg. Sel. Topics Power Electron.*, vol. 3, no. 1, pp. 65–74, Mar. 2015.

[14] N. Liu and T. G. Habetler, "Design of a universal inductive charger for multiple electric vehicle models," *IEEE Trans. Power Electron.*, vol. 30, no. 11, pp. 6378–6390, Nov. 2015.

[15] Q. Chen, S. C. Wong, C. K. Tse, and X. Ruan, "Analysis, design, and control of a transcutaneous power regulator for artificial hearts," *IEEE Trans. Biomed. Circuits Syst.*, vol. 3, no. 1, pp. 23–31, Feb. 2009.

[16] Y. Jiang, L. Wang, Y. Wang, J. Liu, M. Wu, and G. Ning, "Analysis, design, and implementation of WPT system for EV's battery charging based on optimal operation frequency range," *IEEE Trans. Power Electron.*, vol. 34, no. 7, pp. 6890–6905, Jul. 2019.

[17] W. Zhang, S. Wong, C. K. Tse, and Q. Chen, "Design for efficiency optimization and voltage controllability of series–series compensated inductive power transfer systems," *IEEE Trans. Power Electron.*, vol. 29, no. 1, pp. 191–200, Jan. 2014.

[18] Z. Huang, S. Wong, and C. K. Tse, "Design of a single-stage inductive-power-transfer converter for efficient EV battery charging," *IEEE Trans. Veh. Technol.*, vol. 66, no. 7, pp. 5808–5821, Jul. 2017.

[19] W. Zhang, S. Wong, C. K. Tse, and Q. Chen, "Analysis and comparison of secondary series- and parallel-compensated inductive power transfer systems operating for optimal efficiency and load-independent voltage-transfer ratio," *IEEE Trans. Power Electron.*, vol. 29, no. 6, pp. 2979–2990, Jun. 2014.

[20] K. Song, Z. Li, J. Jiang, and C. Zhu, "Constant current/voltage charging operation for series–series and series–parallel compensated wireless power transfer systems employing primary-side controller," *IEEE Trans. Power Electron.*, vol. 33, no. 9, pp. 8065–8080, Sep. 2018.

[21] Z. Huang, S. Wong, and C. K. Tse, "An inductive-power-transfer converter with high efficiency throughout battery-charging process," *IEEE Trans. Power Electron.*, vol. 34, no. 10, pp. 10245–10255, Oct. 2019.

[22] J. Lu, G. Zhu, D. Lin, Y. Zhang, J. Jiang, and C. C. Mi, "Unified load-independent ZPA analysis and design in CC and CV modes of higher order resonant circuits for WPT systems," *IEEE Trans. Transp. Electrific.*, vol. 5, no. 4, pp. 977–987, Dec. 2019.

[23] L. Yang, X. Li, S. Liu, Z. Xu, and C. Cai, "Analysis and design of an *LCCC*/S-compensated WPT system with constant output characteristics for battery charging applications," *IEEE J. Emerg. Sel. Topics Power Electron.*, vol. 9, no. 1, pp. 1169–1180, Feb. 2021.

[24] X. Qu, H. Chu, S. Wong, and C. K. Tse, "An IPT battery charger with near unity power factor and load-independent constant output combating design constraints of input voltage and transformer parameters," *IEEE Trans. Power Electron.*, vol. 34, no. 8, pp. 7719–7727, Aug. 2019.

[25] V. Vu, D. Tran, and W. Choi, "Implementation of the constant current and constant voltage charge of inductive power transfer systems with the double-sided *LCC* compensation topology for electric vehicle battery charge applications," *IEEE Trans. Power Electron.*, vol. 33, no. 9, pp. 7398–7410, Sep. 2018.

[26] D. H. Tran, V. B. Vu, and W. Choi, "Design of a high-efficiency wireless power transfer system with intermediate coils for the on-board chargers of electric vehicles," *IEEE Trans. Power Electron.*, vol. 33, no. 1, pp. 175–187, Jan. 2018.

[27] J. Lu, G. Zhu, D. Lin, Y. Zhang, H. Wang, and C. C. Mi, "Realizing constant current and constant voltage outputs and input zero phase angle of wireless power transfer systems with minimum component counts," *IEEE Trans. Intell. Transp. Syst.*, vol. 22, no. 1, pp. 600–610, Jan. 2021.

[28] R. L. Steigerwald, "A comparison of half-bridge resonant converter topologies," *IEEE Trans. Power Electron.*, vol. 3, no. 2, pp. 174–182, Apr. 1988.

[29] M. Budhia, J. T. Boys, G. A. Covic, and C. Huang, "Development of a single-sided flux magnetic coupler for electric vehicle IPT charging systems," *IEEE Trans. Ind. Electron.*, vol. 60, no. 1, pp. 318–328, Jan. 2013.

[30] A. Zaheer, H. Hao, G. A. Covic, and D. Kacprzak, "Investigation of multiple decoupled coil primary pad topologies in lumped IPT systems for interoperable electric vehicle charging," *IEEE Trans. Power Electron.*, vol. 30, no. 4, pp. 1937–1955, Apr. 2015.

[31] M. F. Menke, Á. R. Seidel, and R. V. Tambara, "LLC LED driver small-signal modeling and digital control design for active ripple compensation," *IEEE Trans. Ind. Electron.*, vol. 66, no. 1, pp. 387–396, Jan. 2019.
[32] S. Tian, F. C. Lee, and Q. Li, "Equivalent circuit modeling of LLC resonant converter," *IEEE Trans. Power Electron.*, vol. 35, no. 8, pp. 8833–8845, Aug. 2020.
[33] S. Li, W. Li, J. Deng, T. D. Nguyen, and C. C. Mi, "A double-sided LCC compensation network and its tuning method for wireless power transfer," *IEEE Trans. Veh. Technol.*, vol. 64, no. 6, pp. 2261–2273, Jun. 2015.
[34] T. Kan, T. Nguyen, J. C. White, R. K. Malhan, and C. C. Mi, "A new integration method for an electric vehicle wireless charging system using LCC compensation topology: Analysis and design," *IEEE Trans. Power Electron.*, vol. 32, no. 2, pp. 1638–1650, Feb. 2017.
[35] L. Bing, L. Wenduo, L. Yan, F. C. Lee, and J. D. Van Wyk, "Optimal design methodology for LLC resonant converter," in *Proc. IEEE Appl. Power Electron. Conf. Expo* ., Mar. 2006, pp. 533–538.
[36] J. Hou, Q. Chen, X. Ren, X. Ruan, S. Wong, and C. K. Tse, "Precise characteristics analysis of series/series-parallel compensated contactless resonant converter," *IEEE J. Emerg. Sel. Topics Power Electron.*, vol. 3, no. 1, pp. 101–110, Mar. 2015.

Zhuhaobo Zhang (Student Member, IEEE) received the B.S. degree in electrical engineering, in 2017, from Zhejiang University, Hangzhou, China, where he is currently working toward the Ph.D. degree in electrical engineering.

His research interests include wireless power transfer, resonant converters, and electric vehicle charging systems.

Shaoting Zheng (Student Member, IEEE) received the B.S. degree in electrical engineering, in 2019, from Zhejiang University, Hangzhou, China, where he is currently working toward the Ph.D. degree in electrical engineering.

His current research focuses on wireless power transfer.

Shiying Luo (Student Member, IEEE) received the B.S. degree in electrical engineering and automation from Harbin Institute of Technology, Harbin, China, in 2019. He is currently working toward the Ph.D. degree in electrical engineering with Zhejiang University, Hangzhou, China.

His research interests include inductive power transfer and resonant converters.

Dehong Xu (Fellow, IEEE) received the B.S., M.S., and Ph.D. degrees from the College of Electrical Engineering, Zhejiang University, Hangzhou, China, in 1983, 1986, and 1989, respectively.

Since 1996, he has been as a Full Professor with the College of Electrical Engineering, Zhejiang University. From June 1995 to May 1996, he was a Visiting Scholar with the University of Tokyo, Tokyo, Japan. From June to December 2000, he was a Visiting Professor with the Center for Power Electronics Systems, Virginia Tech, Blacksburg, VA, USA. From February 2006 to April 2006, he was a Visiting Professor with the ETH Zurich, Zürich, Switzerland. His research interests include power electronics topologies and control, and power conversion for renewable energy and energy saving. He authored or coauthored eight books and more than 270 IEEE journal and conference papers. He holds more than 50 patents.

Dr. Xu was the recipient of seven IEEE journal and conference paper awards. He became an IEEE Fellow in 2013. He was an IEEE PELS Distinguish Lecturer from 2015 to 2018. He was the recipient of the IEEE PELS R. D. Middlebrook Achievement Award in 2016.

Philip T. Krein (Life Fellow, IEEE) received the B.S. degree in electrical engineering and A.B. degree in economics and business from Lafayette College, Easton, PA, USA, in 1978, and the M.S. and Ph.D. degrees in electrical engineering from the University of Illinois at Urbana-Champaign, Champaign, IL, USA, in 1980 and 1982, respectively.

He was an Engineer with Tektronix, Beaverton, OR, USA, and then returned to the University of Illinois at Urbana-Champaign. From 1997 to 1998, he was a Senior Fulbright Scholar with the University of Surrey, Guildford, U.K. From 2003 to 2014, he was the Founder and Director of SolarBridge Technologies, Inc., Austin, TX, USA, a developer of ac photovoltaic panels. From 2016 to 2020, he was an Executive Dean of the Zhejiang University/University of Illinois at Urbana-Champaign Institute, Haining, China. He holds the Grainger Endowed Chair Emeritus in Electric Machinery and Electromechanics at the University of Illinois at Urbana-Champaign and is an Adjunct Distinguished Professor with Zhejiang University, Hangzhou, China. He holds 42 U.S. patents. His research interests include all aspects of power electronics, machines, drives, and electric transportation, with emphasis on nonlinear control approaches.

Dr. Krein was the recipient of the IEEE William E. Newell Power Electronics Award in 2003 and the IEEE Transportation Technologies Award in 2021. He is a Past President of the IEEE Power Electronics Society, a past member of the IEEE Board of Directors, a Past Chair of the IEEE Transportation Electrification Community, and an Associate Editor for the IEEE OPEN JOURNAL OF POWER ELECTRONICS. He is a Registered Professional Engineer in Illinois and Oregon. He is a Fellow of the U.S. National Academy of Inventors and a member of the U.S. National Academy of Engineering.

Hao Ma (Senior Member, IEEE) received the B.S., M.S., and Ph.D. degrees in electrical engineering from Zhejiang University, Hangzhou, China, in 1991, 1994, and 1997, respectively.

Since 1997, he has been a Lecturer, Associate Professor, and Professor with Zhejiang University. From September 2007 to September 2008, he was a Delta Visiting Scholar with the North Carolina State University, Raleigh, NC, USA. He is the Vice Dean of the Zhejiang University/University of Illinois at Urbana-Champaign Institute, Haining, China. He authored two books and authored or coauthored more than 200 technical papers. His research interests include advanced control in power electronics, wireless power transfer, fault diagnosis of power electronic circuits and systems, and application of power electronics.

Dr. Ma is currently the Vice-President of China Power Supply Society. He was the AdCom member of the IEEE Industrial Electronics Society, the Technical Program Chair of the IEEE International Symposium on Industrial Electronics 2012, IEEE International Power Electronics and Application Conference and Exposition 2014, IEEE International Power Electronics and Application Conference and Exposition 2018, and IEEE International Power Electronics and Application Symposium 2021.